NANO · MICRO small
www.small-journal.com

Reinforcing the Induction of Immunogenic Cell Death Via Artificial Engineered Cascade Bioreactor-Enhanced Chemo-Immunotherapy for Optimizing Cancer Immunotherapy

Kai Sun, Jinzhong Hu, Xiangyu Meng, Yunfeng Lei, Xuezhong Zhang, Zhuoxuan Lu, Liming Zhang, and Zhifei Wang**

Traditional chemo-immunotherapy can elicit T cell immune response by inducing immunogenic cell death (ICD), however, insufficient ICD limits the lasting antitumor immunotherapeutic efficacy. Herein, tadpole–ovoid manganese-doped hollow mesoporous silica coated gold nanoparticles (Au@HMnMSNs) as biodegradable catalytic cascade nanoreactors are constructed to generate intratumoral high-toxic hydroxyl radicals combined with DOX and Aspirin (ASA) for enhancing the induction of ICD and maturation of dendritic cells (DCs). The released Mn^{2+} can catalyze endogenous H_2O_2 to hydroxyl radicals, while internal gold nanoparticles mimetic glucose oxidase (GOx) converted glucose into H_2O_2 to accelerate the generation of hydroxyl radicals. On the other hand, tadpole oval-structured Au@HMnMSNs can avoid the inactivation of gold nanoparticles due to strong protein adsorption. The introduction of ASA is to recruit DCs and cytotoxic T lymphocytes (CTLs) to tumor sites and restrain the intratumoral infiltration of immunosuppressive cells by decreasing the expression of prostaglandin E2 (PGE_2). Accordingly, this work presents a novel insight to introduce GOx-like catalytic cascade ICD nano-inducer into antitumor immunotherapy for synergistic tumor therapy.

1. Introduction

Cancer immunotherapy, which can activate and boost the innate immune system to generate antitumor immunity to combat tumor growth and metastasis, is considered to be a promising treatment strategy for the future.[1,2] However, due to the low immune response rate, the efficacy of immunotherapy is much lower than expectations. Moreover, tumor microenvironment (TME) can promote virtue of immune evasion and immunosuppression to avoid immune attack. Cancer immune cycle is the process of cancer immunotherapy through a series of steps to initiate antitumor immune response. Recently, more research has begun to focus on remodulating the immunosuppression tumor microenvironment (ITM) to achieve better antitumor immunotherapy effects.[3,4]

Immunogenic cell death (ICD) plays a crucial role in activating the immune response.[5,6] The dying tumor cells undergoing ICD can release tumor-associated antigens (TAAs) and damage-associated molecular patterns (DAMPs), including the surface exposure of calreticulin (CRT) and high mobility group box 1 (HMGB1) release to potentiate the recruitment and antigen presentation of antigen presenting cells (APCs) and boost the infiltration of cytotoxic T lymphocytes (CTLs) into tumor tissue.[7–9] The process could induce the maturation of dendritic cells (DCs), which are one of the most important APCs, to initiate innate and adaptive immunity.[10] Therefore, the phenotypic and functional maturation of DCs determine the therapeutic effect of antitumor immune response. However, inherent troubles with DCs and the low level of ICD induction seriously block antitumor efficiency in immunosuppressive microenvironment.[11–13]

Cyclooxygenase-2 (COX-2) has been confirmed to be a key factor in the immune suppression by upregulating prostaglandin E_2 (PGE_2) in tumor cells.[14,15] High COX-2 expression could cause tumor cells to hinder the migration of DCs, strengthen the barrier between T cells and tumor cells, and recruit more immunosuppressive cells.[16–18] Thus, inhibition of COX-2 can reverse tumor immunosuppression and effectively improve the efficiency of tumor cells elimination. As an FDA-approved anti-inflammatory drug, Aspirin (acetylsalicylic acid, ASA) is one of the COX inhibitors.[19] In previous studies, it was found that the introduction of ASA would increase tumor infiltrating lymphocytes in chemo-preventive treatment.[20–22] Nevertheless, the down-regulation of COX-2/PGE_2 expression of ASA has not been studied in the process of DCs maturation induced by ICD to stimulate potential anti-tumor immunity. Although traditional chemo-drugs kill tumor cells by apoptosis or necrosis, and induce ICD to stimulate the maturation of DCs, the level of ICD produced by chemo-drugs alone is

K. Sun, J. Hu, X. Meng, Y. Lei, X. Zhang, Prof. Z. Wang
School of Chemistry and Chemical Engineering
Southeast University
Nanjing 211189, People's Republic of China
E-mail: zfwang@seu.edu.cn
Prof. Z. Lu, Prof. L. Zhang
Key Laboratory of Tropical Translational Medicine of Ministry of Education & Hainan Provincial Key Laboratory of Tropical Medicine
Hainan Medical University
Haikou 571199, People's Republic of China
E-mail: lmzhang1980@163.com
The ORCID identification number(s) for the author(s) of this article can be found under https://doi.org/10.1002/smll.202101897.

DOI: 10.1002/smll.202101897

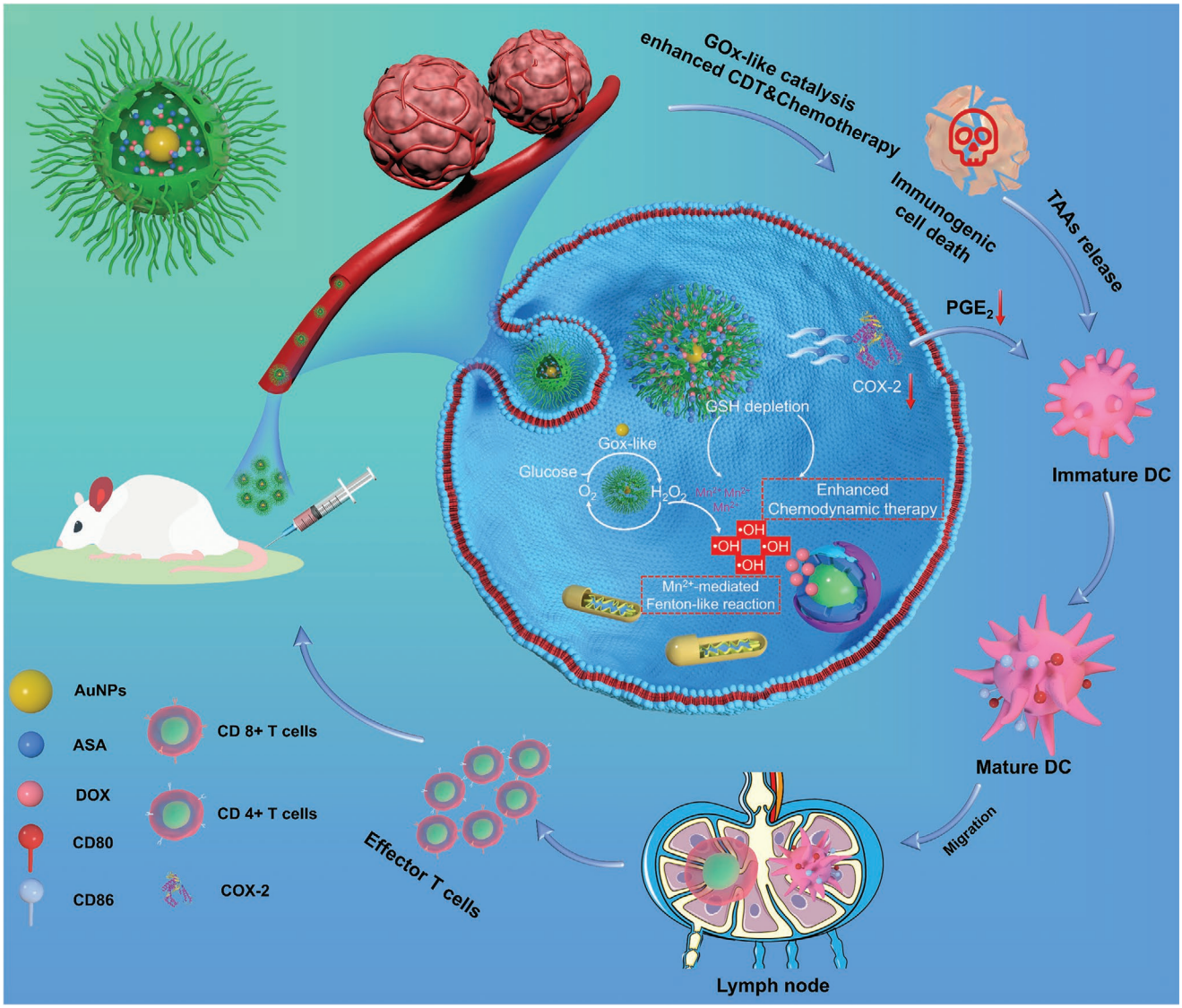

Scheme 1. Schematic diagram of PEGylated Au@HMnMSNs ICD nanoinducers for eliciting potent antitumor immunotherapeutic efficacy.

inadequate, which impedes the activation of cytotoxic T lymphocytes and infiltration into the tumor tissue.[23–25]

Herein, we first constructed a tadpole–ovoid manganese-doped hollow mesoporous silica coated gold nanoparticle (Au@HMnMSN) to reinforce the induction of ICD and maturation of DCs after loading doxorubicin (DOX) and ASA (**Scheme 1**). Au@HMnMSNs, as cascade nanoreactors, could be degraded by consuming antioxidant glutathione (GSH) to release Mn^{2+} for Fenton-like reaction to generate highly toxic hydroxyl radicals (•OH) in TME. In a previous study,[26–28] it has been confirmed that gold nanoparticles can harness glucose oxidase (GOx) like catalytic activity to decompose glucose into gluconic acid and H_2O_2. Interestingly, Au@HMnMSNs could convert endogenous H_2O_2 into O_2 to improve the GOx-like catalytic activity of gold nanoparticles. Meanwhile, tadpole oval-structured Au@HMnMSNs could avoid the inactivation of gold nanoparticles due to strong protein adsorption in biological fluids and promote further GOx-like catalysis.[29] As a result, the regeneration of H_2O_2 could dedicate to Fenton-like reaction for achieving GOx-like catalysis enhanced chemodynamic therapy (CDT), which combined with chemotherapy to induce sufficient ICD for release of TAA, and then stimulate potent systemic antitumor immunity. On the other hand, the introduction of ASA was to remodel ITM by restraining the expression of PGE_2, which could promote the recruitment and maturation of DCs into TME and decrease the barrier between CTLs and tumor cells. Synergistic GOx-like catalysis-enhanced CDT combined with chemotherapy could provide a promising strategy to amplify antitumor immunotherapy effects via inducing sufficient ICD.

2. Results and Discussion

2.1. Synthesis and Characterization

Tadpole–ovoid Au@HMnMSNs with tumor microenvironment responsive degradation behavior were fabricated via a

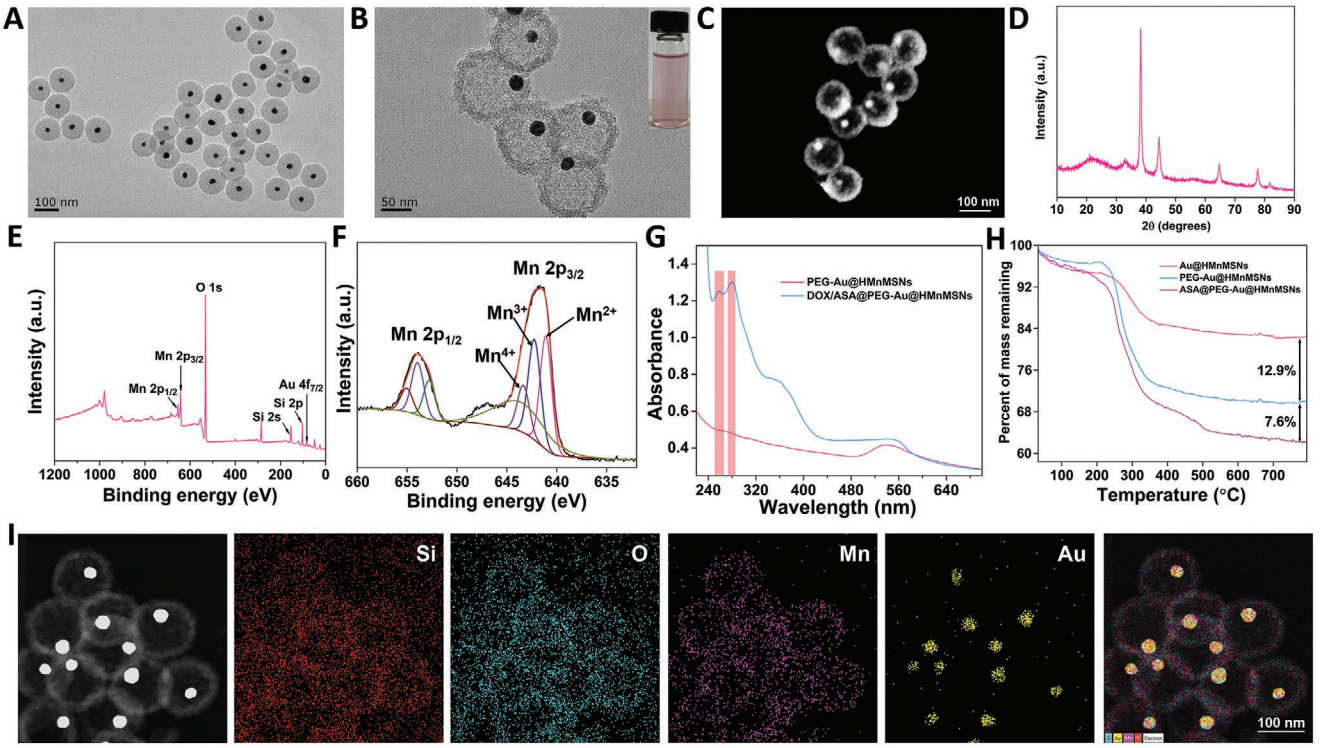

Figure 1. TEM images of A) Au@MSNs and B) Au@HMnMSNs. Inset: A photograph of Au@HMnMSNs in the PBS soulution. C) SEM images of Au@HMnMSNs. D) XRD pattern and E,F) XPS spectrum of Au@HMnMSNs. G) UV–vis spectra of PEGylated Au@HMnMSNs before and after encapsulation with DOX and ASA. H) The change of TGA curves. I) EDS elemental mapping of Si, O, Mn, and Au of Au@HMnMSNs.

two-step procedure. As shown in **Figure 1**A, Au@MSNs with single gold core-mesoporous silica shell were prepared using a facile one-pot method with an average size of 105 nm. Then, Au@MSNs doped Mn into mesoporous silicon shell under high-temperature hydrothermal condition to form hollow mesoporous Au@HMnMSNs, indicating that Au@HMnMSNs with a uniform size of 120 ± 5 nm containing ≈18 nm gold core were successfully prepared (Figure 1B,C). The wide-angle X-ray diffraction pattern (XRD) of the Au@HMnMSN showed several sharp peaks (38.2°, 44.4°, 64.7°, 77.7°, and 81.7°) and broadened peaks (21.3°, 33.2°, and 56.2°), which were respectively assigned to cubic metal of gold (JCPDS 04–0784) and amorphous state of $Mn_x(SiO_4)_y$ (JCPDS 33–0904) (Figure 1D). Furthermore, the element mapping and energy dispersive X-ray spectroscopy (EDS) of Au@HMnMSN were conducted to confirm that Si, O, Mn, and Au were expectedly distributed within the Au@HMnMSN, which manifested the successful synthesis of Au@HMnMSN (Figure 1I; Figure S1, Supporting Information). The results also showed that the mass ratios of Au and Mn were nearly 15.13% and 13.24%. The X-ray photoelectron spectroscopy (XPS) indicated that the main peak of Mn $2p_{3/2}$ was divided into three characteristic peaks at 641.08, 642.38, and 643.68 eV, each of which respectively corresponded to the valence of Mn^{2+}, Mn^{3+}, and Mn^{4+} (Figure 1E,F). Besides, Mn-doped hollow mesoporous silica nanoparticles (HMnMSNs) were successfully prepared (Figure S2, Supporting Information).

The PEGylated Au@HMnMSNs (PEG–Au@HMnMSNs) could increasingly accumulate into tumor tissue by enhanced permeability and retention (EPR) effect and overcome the immunogenicity of the host's immune system.[30] After surface PEGylation of Au@HMnMSNs through amidation reaction, the hydrodynamic sizes were measured from 115 to 170 nm and the zeta potential had changed (Figure S3, Supporting Information). The prepared PEG–Au@HMnMSNs was also verified by the Fourier transform infrared (FT-IR) spectroscopy and thermogravimetric analysis (TGA) curves (Figure S4, Supporting Information; Figure 1H). With the continuous surface modification of the nanoparticles, the absorption values of gold nanoparticle at 535 nm were decreased under the same concentration (Figure S5, Supporting Information), which manifested the formation of PEG–Au@HMnMSNs. Subsequently, the N_2 adsorption–desorption isotherm and pore size distribution of PEG–Au@HMnMSNs were as shown in Figure S6, Supporting Information and the surface area and average pore size were 266.63 m^2 g^{-1} and 2.8 nm, respectively, exhibiting the presence of mesoporous structure. ASA, which could inhibit the expression of COX-2 as a representative drug for New Uses of Old Drugs, and chemotherapy drug DOX were co-loaded into PEG–Au@HMnMSNs by strong π–π stacking interaction and physical absorption. As shown in Figure 1G, DOX/ASA-loaded PEG-Au@HMnMSNs showed two strong absorption peaks at 256 and 278 nm compared with PEG–Au@HMnMSNs, which were attributed to the presence of DOX and ASA, respectively. In addition, the drug loading capacities of ASA and DOX were computed to be 7.6% and 9.5% via physical absorption and strong π–π stacking interaction according to TGA and the UV–vis standard curve (Figure 1H; Figure S8, Supporting Information). DOX/ASA@PEG-Au@HMnMSNs also exhibited

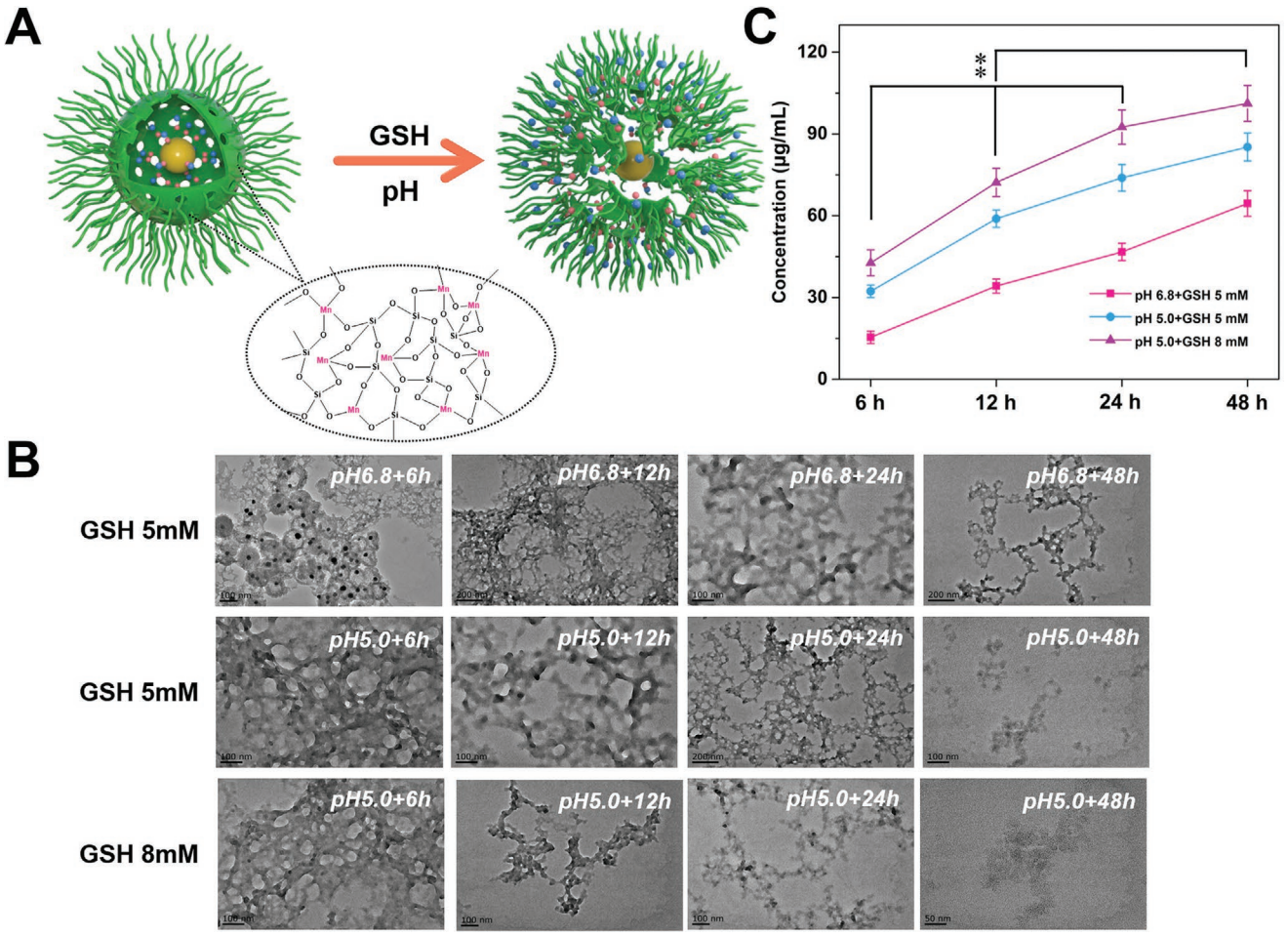

Figure 2. Biodegradation of PEG–Au@HMnMSNs in SBF solution. A) Schematic description of ASA/DOX-release from PEG–Au@HMnMSNs in the biodegradation process (inset: chemical composition). B) TEM images of PEG–Au@HMnMSNs after degradation and C) corresponding accumulated releasing profiles of Mn element from PEG–Au@HMnMSNs under different conditions. $n = 3$, mean ± SD; $^{**}P < 0.01$.

excellent blood compatibility by hemolysis assay, which could remain stable in blood circulation (Figure S9, Supporting Information).

2.2. Tumor Microenvironment Responsive Biodegradation Behavior

Since Mn—O bonds were sensitive to acidic and reducing tumor microenvironment, PEG—Au@HMnMSNs with manganese embedded into the silicon shell could accelerate the process of biodegradation.[31,32] To imitate acidic endo/lysosomal (pH 5.0–6.5/4.5–5.0) and overexpressed GSH of tumor microenvironment,[33] simulated body fluid (SBF) solutions with different GSH concentrations (5 and 8 mM) and pH values (6.8 and 5.0) were used to investigate the degradation of PEG–Au@HMnMSNs at various time intervals (**Figure 2**). The morphology of PEG–Au@HMnMSNs was visually observed by TEM, and the amounts of released Mn were determined by ICP-MS analysis. The morphology of PEG–Au@HMnMSNs stepwise cracked with the increase of time, GSH concentration, and acidity via TEM. The release rate of Mn in the group with 8 mM of GSH and pH 5.0 was significantly higher than the others up to 42.7, 72.2, 92.5, and 101.2 μg mL^{-1} over time, and gold nanoparticles were completely exposed to the SBF solution for enhancing endogenous H_2O_2 concentration through the GOx-like catalytic oxidation of glucose to H_2O_2 and gluconic acid. In addition, the dialysis method was used to investigate the drug release of PEG–Au@HMnMSNs. Because acidic and reducing conditions could accelerate the degradation of PEG–Au@HMnMSNs to release drugs, the difference between accumulative release of DOX and ASA was not great. Besides, the release of DOX and ASA within 24 h was up to 79.85% and 84.85% under PBS solution with 5 mM of GSH and pH 5.0, which was signally higher than other condition groups (Figure S10, Supporting Information).

2.3. GSH Depletion-Enhanced •OH Generation

High expression of GSH in tumor cells could weaken the efficacy of CDT-based treatments. In view of the sensitive property of PEG–Au@HMnMSNs to acidic and reducing environment, GSH consumption detection assay was investigated

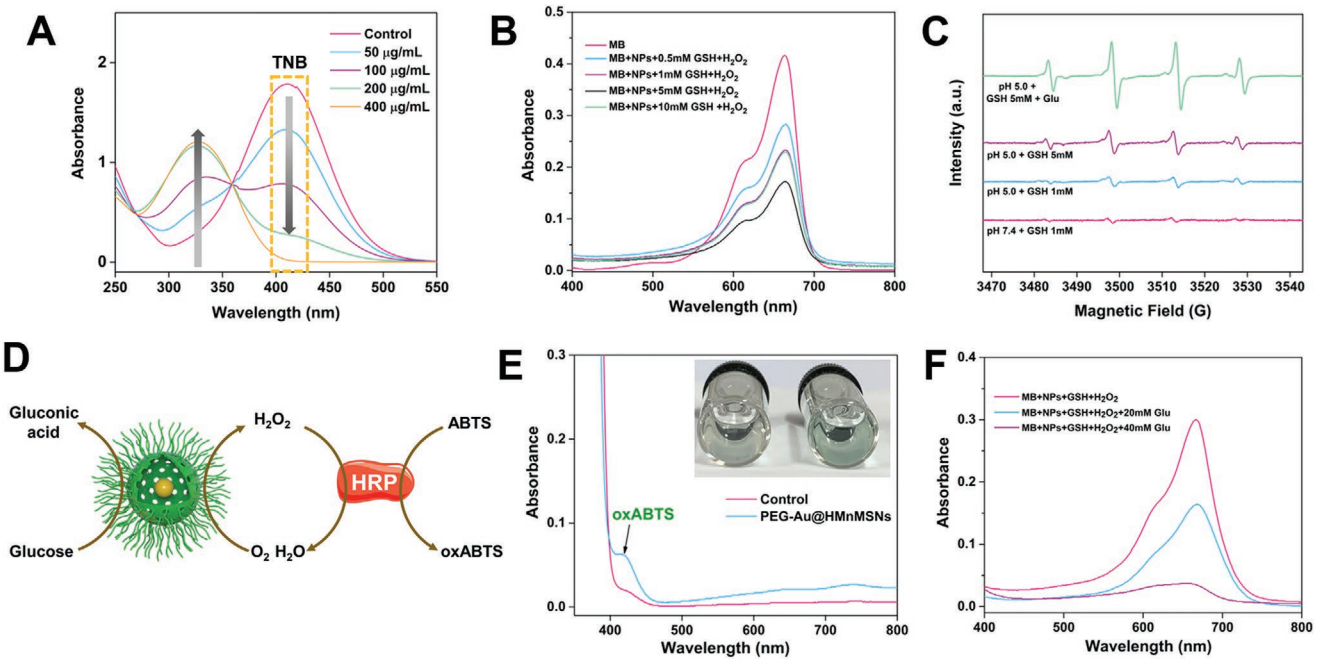

Figure 3. A) Degradation of DTNB by remanent GSH after treating with different concentration of PEG–Au@HMnMSNs in the PBS solutions. B) MB consumption by H_2O_2 plus GSH-treated PEG–Au@HMnMSNs in the $NaHCO_3/CO_2$ buffer solutions. C) ESR spectra of demonstrating $^{\bullet}OH$ generation of PEG–Au@HMnMSNs. D) Schematic graph describing the PEG–Au@HMnMSNs as GOx-like mimetics. E) UV–vis spectra of PEG–Au@HMnMSNs after incubation. Inset: Corresponding actual photographs. F) MB degradation by H_2O_2 plus GSH-treated PEG–Au@HMnMSNs after addition of glucose.

using an indicator 5,5′-dithiobis (2-nitrobenzoic acid) (DTNB), which could react with GSH to GSSH and TNB. As shown in **Figure 3**A, GSH could react with different concentration of PEG–Au@HMnMSNs (50, 100, 200, and 400 μg mL^{-1}). As the concentration of PEG–Au@HMnMSNs increased, more GSH could be consumed. As a result, remanent GSH reacting with DTNB could produce less TNB with an absorption peak at 412 nm in acidic PBS solution, revealing the consumption of GSH by PEG–Au@HMnMSNs to release Mn^{2+} for Fenton-like catalysis.

Another major feature was the overexpression of H_2O_2 in tumor cells, and released Mn^{2+} could convert endogenous H_2O_2 into highly toxic $^{\bullet}OH$ with the assistance of HCO_3^-/CO_2 physiological buffer.[34,35] As shown in Figure 3B, methylene blue (MB) was degraded by $^{\bullet}OH$ as an indicator, which could be used to detect the production of $^{\bullet}OH$. As the concentration of GSH increased from 0 to 5 mM, the MB was degraded in the presence of GSH-response PEG–Au@HMnMSNs and H_2O_2. However, the degradation of MB was reduced at 10 mM of GSH, indicating GSH could restrict the CDT efficiency by eliminating the generated $^{\bullet}OH$. As the concentration of GSH increased from 0 to 10 mM, the absorbance wavelength of MB at 665 nm barely changed, to confirm that GSH and H_2O_2 did not cause the reduction of MB signal (Figure S11, Supporting Information). Besides, 5,5-dimethyl-1-pyrroline-*N*-oxide (DMPO), as a trapping agent, was used to directly capture short-lived $^{\bullet}OH$ by electron spin resonance measurement (ESR). The characteristic signals of $^{\bullet}OH$ (1:2:2:1) could be obviously observed after treating with H_2O_2 and released Mn^{2+} under different conditions (Figure 3C), further proving the GSH depletion-reinforced $^{\bullet}OH$ production.

2.4. GOx-Like Catalytic Performance Assessments of PEG–Au@HMnMSNs

Before degradation, PEG–Au@HMnMSNs could protect the surface of gold nanoparticles from passivation and impact further catalysis in TME. A horseradish peroxidase (HRP)-based colorimetric measurement was utilized to investigate the GOx-like catalytic oxidation of glucose to H_2O_2 (Figure 3D,E). The appearance of characteristic green color of oxABTS (maximum absorbance at 405 nm) verified the enzymatic activity of Au nanozyme. As shown in Figure 3C, the characteristic signals of $^{\bullet}OH$ (1:2:2:1) were remarkably enlarged. In view of overexpression of in tumor cells, when 20 and 40 mM concentrations of glucose along with low concentration of H_2O_2 were respectively added, the MB was degraded more, indicating that more hydroxyl radicals were generated due to the increased level of H_2O_2 by catalytic oxidation of glucose (Figure 3F).

2.5. GOx-Like Catalysis-Enhanced Chemodynamic Activity

Inspired by the excellent properties of PEG–Au@HMnMSNs to generate $^{\bullet}OH$, GOx-like catalysis-enhanced chemodynamic activity was analyzed in vitro. The cascade nanozyme was expected to catalyze glucose to produce H_2O_2 and gluconic acid, consuming oxygen. The intracellular pH and O_2 variation were investigated to uncover the GOx-like catalytic reaction of PEG–Au@HMnMSNs. The fluorescence intensity of BCECF AM could be quenched at acidic environment. As shown in **Figure 4**A,B, 4T1 cells treated with PEG–Au@HMnMSNs qualitatively and quantitatively indicated the weakest fluorescence

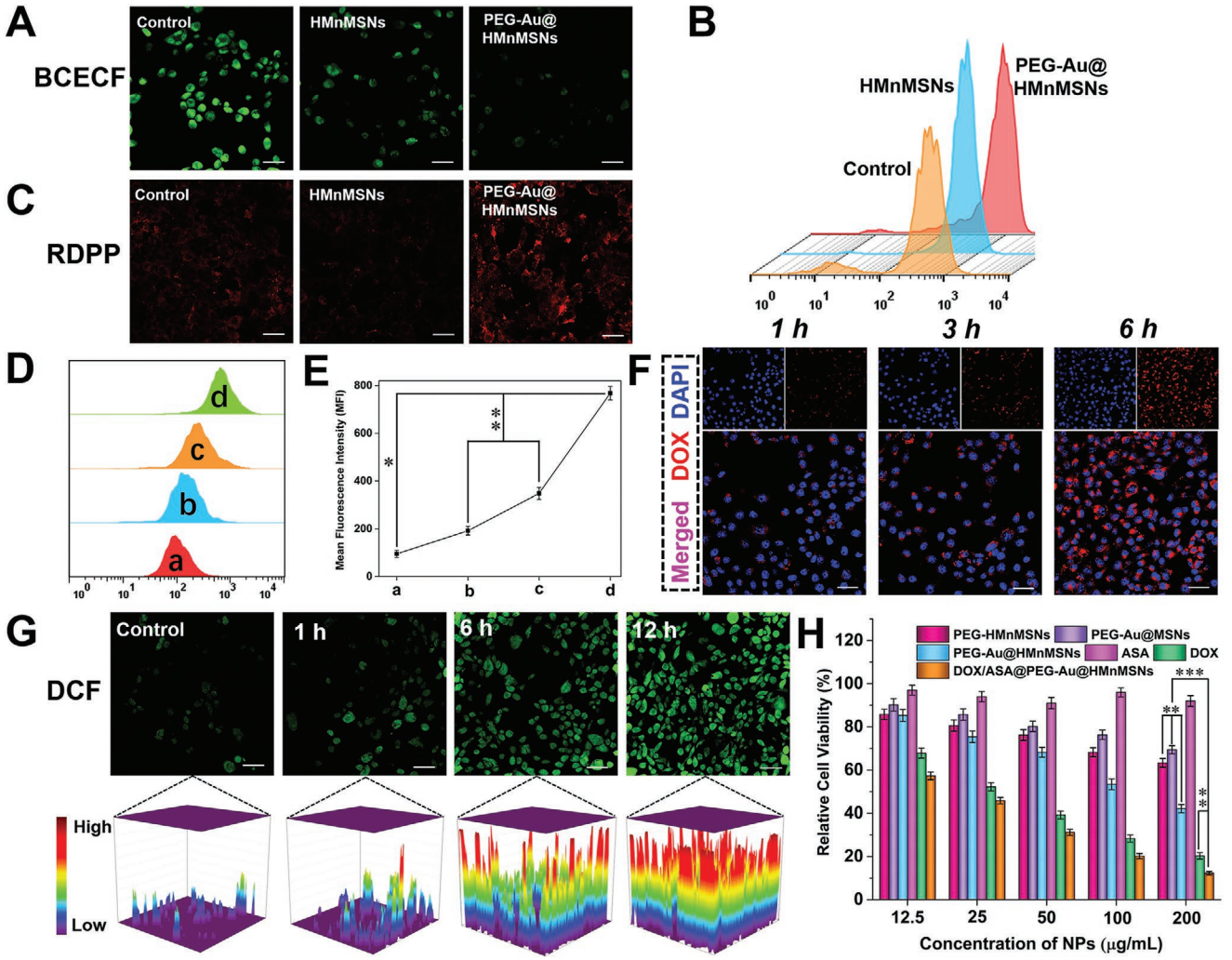

Figure 4. A) The fluorescent images of 4T1 cells incubated with PBS, HMnMSNs, and PEG–Au@HMnMSNs after BCECF-AM staining for pH measurements. Scale bar: 40 μm. B) Flow cytometry assays of pH levels in 4T1 cells. C) The fluorescent images of 4T1 cells incubated with PBS, HMnMSNs, and PEG–Au@HMnMSNs after RDPP staining. Scale bar: 40 μm. D) Flow cytometry assays of ROS levels in 4T1 cells, and E) corresponding mean fluorescence intensity of PBS (a), PEG-Au@HMnMSNs (b), DOX/ASA@PEG–Au@HMnMSNs (c), and DOX/ASA@PEG–Au@HMnMSNs plus glucose (d). F) CLSM images of 4T1 cells after incubation with PEG–Au@HMnMSNs. DAPI (nuclei, blue) and DOX fluorescence (red). Scale bar: 40 μm. G) CLSM and corresponding surface plot images of ROS levels induced by PEG–Au@HMnMSNs. Scale bar: 40 μm. H) Relative cell viability of 4T1 cells treated with different formulations via CCK-8 assay. $n = 3$, mean ± SD; $^{*}P < 0.05$; $^{**}P < 0.01$; $^{***}P < 0.001$.

signal compared with PBS and HMnMSNs groups without function of Au nanozyme, displaying the formation of gluconic acid to cause a decrease in the intracellular pH. RDPP, as O_2 probe, could increase the signal of red fluorescence in the absence of O_2. Compared with PBS and HMnMSNs groups, 4T1 cells treated with PEG–Au@HMnMSNs showed stronger red fluorescence, reflecting the GOx-like catalytic reaction that consumed the glucose and O_2 (Figure 4C).

GOx-like catalysis-enhanced intracellular reactive oxygen species (ROS) levels were visualized by 2′,7′-dichlorodihydrofluorescein diacetate (DCF-DA), which could be oxidized to green fluorescent 2′,7′-dichlorodihydrofluorescein (DCF) by the presence of ROS.[36] DCF fluorescence induced PEG–Au@HMnMSNs in 4T1 cells was gradually stronger with the prolonged incubation time (1, 6, 12 h) (Figure 4G). To further investigate the function of AuNP (GOx-mimic enzyme) and Mn (Fenton catalyst) in cancer therapy, we also measured the experiment with intracellular ROS enhanced by treatment with PEG–Au@MSNs, PEG–HMnMSNs, and PEG–Au@HMnMSNs in 4T1 cells (Figure S13, Supporting Information). DCF fluorescence induced by PEG–Au@MSNs and PEG–HMnMSNs in 4T1 cells was both stronger than the control group, which respectively attributed to the GOx-like catalyzed H_2O_2 production in the presence of AuNPs, and the generation of $^{\bullet}OH$ by Mn^{2+} catalyst. However, DCF fluorescence intensity induced by combined PEG–Au@HMnMSNs in 4T1cells was the strongest, indicating the function of catalytic cascade nanoreactors. Flow cytometry was used to quantitatively analyze the effects of loading drugs and glucose on intracellular ROS levels, and the clear shift could be observed in Figure 4D,E, further suggesting GOx-like catalysis-enhanced chemodynamic activity. Furthermore, Figure S14, Supporting Information clarified the

changes of H_2O_2 level in 4T1 cells for 24 h of incubation. ASA and DOX could promote the generation of endogenous H_2O_2. However, after the introduction of PEG–Au@HMnMSNs, the level of H_2O_2 was decreased, which was due to the release of Mn^{2+} catalyzing H_2O_2 to produce highly toxic $^{\bullet}OH$.

2.6. Cellular Uptake and Cytotoxicity Evaluation in Vitro

To deliver agents into tumor cells for efficient tumor treatment, the cellular uptake behavior of PEGylated Au@HMnMSNs was designed to detect on 4T1 cells. As displayed in Figure 4F, the red fluorescence from DOX-loaded PEG–Au@HMnMSNs and the blue fluorescence DAPI staining cell nucleus revealed prominent overlay with the extension of incubation time. Flow cytometry was also utilized to quantify the overlay of fluorescence (Figure S15, Supporting Information), both verifying the internalization of PEG–Au@HMnMSNs via endocytosis.

In vitro GOx-like catalysis-enhanced CDT combined with chemotherapy of 4T1 cells was investigated via CCK-8 assay to evaluate the inherent CDT enhanced effect of PEG–Au@HMnMSNs. As shown in Figure 4H, all formulations except the ASA group displayed a dose-dependent cytotoxicity to 4T1 cells. PEG–Au@HMnMSNs showed a lower cell inhibition rate compared with PEG–HMnMSNs and PEG–Au@MSNs due to the lack of gold nanozyme and Mn catalyst, respectively. However, it showed no obvious cytotoxicity to normal liver cells L-02 under different concentration (Figure S16, Supporting Information). It's worth noting that the administered ASA and DOX doses were calculated according to the drug loading capacity of PEG–Au@HMnMSNs. After introduction of DOX and ASA, DOX/ASA@PEG–Au@HMnMSNs exhibited a distinct inhibition rate. The flow cytometry and live (green)/dead (red) cells staining assay further confirmed potential enhancement effect of DOX/ASA@PEG–Au@HMnMSNs in inducing apoptosis of 4T1 cells to cause a higher cell mortality than single CDT (Figures S17 and S18, Supporting Information).

2.7. ICD-Induced Immune Activation

Such synergistic GOx-like catalysis-enhanced CDT combined with chemotherapy not only kills cancer cells, but more importantly, it could activate antitumor immune response as an ICD nano-inducer to remodulate the ITM and achieve better antitumor immunotherapy effects. CRT, as a dominant biomarker during ICD, acts as an "eat me" signal to guide DCs to take up the dying tumor cells. And HMGB1, another surrogate biomarker for ICD-associated immunogenicity, can stimulate DCs maturation and antigen presentation.[37,38] As displayed in **Figure 5**, the CRT exposure and HMGB1 release in 4T1 cells were assessed. DOX/ASA@PEG–Au@HMnMSNs-treated 4T1 cells could more observably augment the expression level of CRT (higher green fluorescence intensity), compared with PBS, HMnMSNs, DOX/ASA, and PEG–Au@HMnMSNs treatments (Figure 5A). Flow cytometry was further utilized to confirm the high expression of CRT induced by DOX/ASA@PEG–Au@HMnMSNs, quantitatively (Figure 5B; Figure S19, Supporting Information). The increasing expression of CRT was consistent with the cytotoxicity assay, indicating that GOx-like catalysis-enhanced CDT combined with chemotherapy could induce ICD. HMGB1 distributes in the nucleus of the normal cells, but it can migrate outside of the tumor cells undergoing ICD. The amounts of HMGB1 in the supernatants were detected by a HMGB1 ELISA Kit. The HMGB1 release of DOX/ASA@PEG–Au@HMnMSNs group was 402 pg mL^{-1}, which was 1.37-fold,1.67-fold, 2.98-fold, and 4.63-fold higher than that of the PEG–Au@HMnMSNs, DOX/ASA, HMnMSNs, and control groups, respectively (Figure S20, Supporting Information). Furthermore, the expression level of HMGB1 was upregulated with DOX/ASA@PEG–Au@HMnMSNs treatment by western blot (Figure 5C).

Given the satisfied ICD-induction results, the immunogenicity of the tumor cells was evaluated by acting on DCs maturation after various treatments in vitro. DCs maturation could be verified by costimulatory molecules CD80 and CD86, which were considered as markers to elicit T cell-mediated immune responses.[39] The DCs maturation frequency (CD11c+CD80+CD86+) of the control group was 8.64%, which sharply increased to 57.1% after DOX/ASA@PEG–Au@HMnMSNs-treated BMDCs by flow cytometry (Figure 5D). During DCs maturation, other types of immune cells were regulated by releasing cytokines, including interleukin 6 (IL-6, an important marker of humoral immunity), interleukin 12p70 (IL-12p70, important marker of innate immunity), interferon γ (IFN-γ, positive role in the cytotoxic functions of CTLs), and tumor necrosis factor α (TNF-α, important marker of cellular immunity). As displayed in Figure 5E, the highest secretion levels of IL-6, IL-12p70, IFN-γ, and TNF-α could be examined in DOX/ASA@PEG-Au@HMnMSNs-treated supernatant by using mouse inflammation kit. In contrast, the level of interleukin 10 (immunosuppression cytokine) was reduced.

Although the maturation of DCs were crucial initiators of innate and adaptive immune responses, the overexpressed PGE_2 impeded the migration of DCs, strengthened the barrier between T cells and tumor cells, and recruited more immunosuppressive cells. A well-known anti-inflammatory drug ASA improved the immune microenvironment by the inhibition of COX-2 expression and secretion of PGE_2.[14,15,19] As shown in Figure 5F,G, the prohibitive expression level of ASA on COX-2 and PGE_2 was detected by western blot and ELISA in tumor cells (4T1) and tumor-associated macrophages (RAW264.7). The expression level of COX-2 was observably decreased in 4T1 and RAW264.7 as the concentration of ASA increased. Moreover, the level of COX-2 was down-regulated caused by DOX/ASA@PEG–Au@HMnMSNs greater than that induced by control, ASA, DOX, and PEG–Au@HMnMSNs in 4T1 cells. The secretions of PGE_2 in the supernatants of 4T1 cells were quantitatively calculated by ELISA, which was consistent with the results of COX-2 protein expression. It indicated that ASA could effectively inhibit the expression level of COX-2 and PGE_2.

2.8. In Vivo Biodistribution and Infiltration of CD8+ and CD4+ T Lymphocytes

We further evaluated the in vivo biodistribution of PEG–Au@HMnMSNs in the 4T1 tumor-bearing female BALB/c mice, via

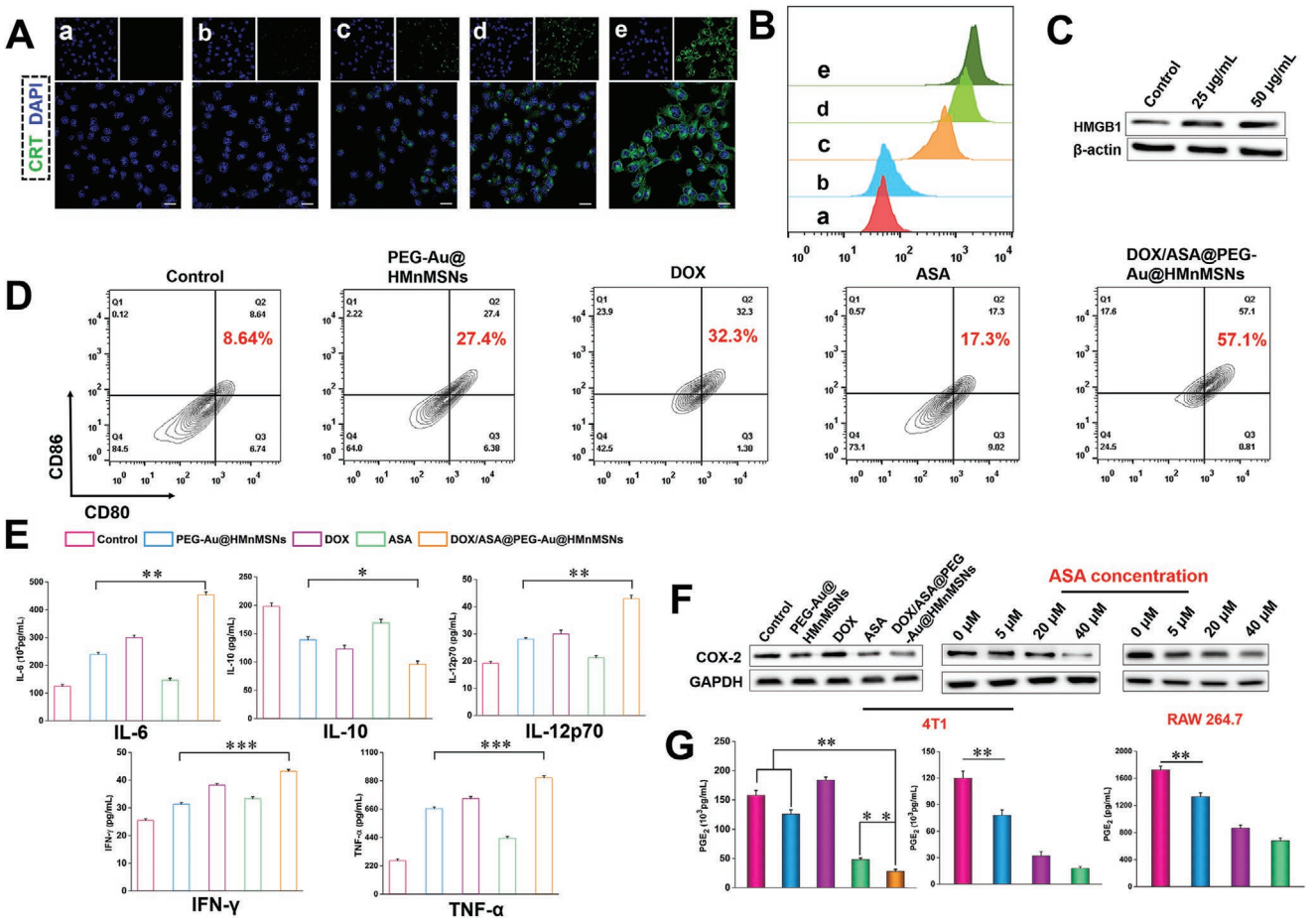

Figure 5. A) CLSM images and B) flow cytometric detection of CRT exposure on the surface of 4T1 cells treated with PBS (a), HMnMSNs (b), DOX/ASA (c), PEG–Au@HMnMSNs (d), and DOX/ASA-loaded PEG-Au@HMnMSNs (e). Scale bar: 20 μm. C) Western blot analysis of released HMGB1 from the 4T1 cells into the extracellular supernatant. D) Expression levels of surface molecules (CD80/CD86) on BMDCs after treatments by flow cytometry analysis (gated on CD11c+). E) Quantification of cytokine production via using mouse inflammation kit for IL-10, IL-12p70, IL-6, IFN-γ, and TNF-α analysis. F,G) Levels of COX-2 expression and PGE_2 secretion in 4T1 cells after different treatments. $n = 3$; $^*P < 0.05$; $^{**}P < 0.01$; $^{***}P < 0.001$.

intravenous injection of Cy5.5-labeled PEG–Au@HMnMSNs and observation by IVIS small animal imaging system at predetermined time intervals. As shown in **Figure 6**A, Cy5.5-labeled nanoparticles exhibited increasing fluorescence in tumor sites with the prolonged injection time (0.5, 3, 12, and 24 h), and the fluorescence intensity reached a maximum within 12 h, indicating high accumulation and long retention time around tumor sites. The mice were sacrificed to obtain main organs and tumors for ex vivo fluorescence imaging after 24 h of injection. The fluorescence intensity at the tumor site was higher than other main organs.

To evaluate GOx-like catalysis-enhanced CDT combined with chemotherapy for synergistic antitumor effect, the infiltration of CD8+/CD4+ cytotoxic T lymphocytes (CTLs) were analyzed by flow cytometry in tumor. CD8+ T cells were one of most significant immune cells to limit tumor progression and induce CTLs killing cancer cells. CD4+ T cells played a vital role in the regulation of adaptive immunities.[40] As shown in Figure 6B, the population of cytotoxic CD8+ and helper CD4+ T cells were remarkably increased in the DOX/ASA@PEG–Au@HMnMSNs group compared with monotherapy, manifesting the reinforcement of innate antitumor immune responses. In addition, the immunofluorescent examinations of the tumor sections with CD8+ and CD4+ staining further verified the previous results (Figure 6D). Meanwhile, the immunohistochemical and immunofluorescent analysis of the sections confirmed that DOX/ASA@PEG–Au@HMnMSNs significantly decreased the expression level of COX-2 and promoted CRT exposure compared with other treatments, which activated antitumor immune response to achieve better potential antitumor immunotherapy effects. To further study the effect of independent loading of DOX or ASA in PEG–Au@HMnMSNs on the COX-2 suppression and antitumor immune response, the immunohistochemical and immunofluorescent analyses of the sections were employed in Figure S21, Supporting Information. When ASA was introduced into PEG–Au@HMnMSNs, DOX/ASA-loaded PEG–Au@HMnMSNs and ASA-loaded PEG–Au@HMnMSNs significantly decreased the expression level of COX-2, compared with DOX-loaded PEG–Au@HMnMSNs, which indicated COX-2 suppression induced potential anti-cancer immunotherapy. In addition, the immunofluorescent examinations of the tumor sections with

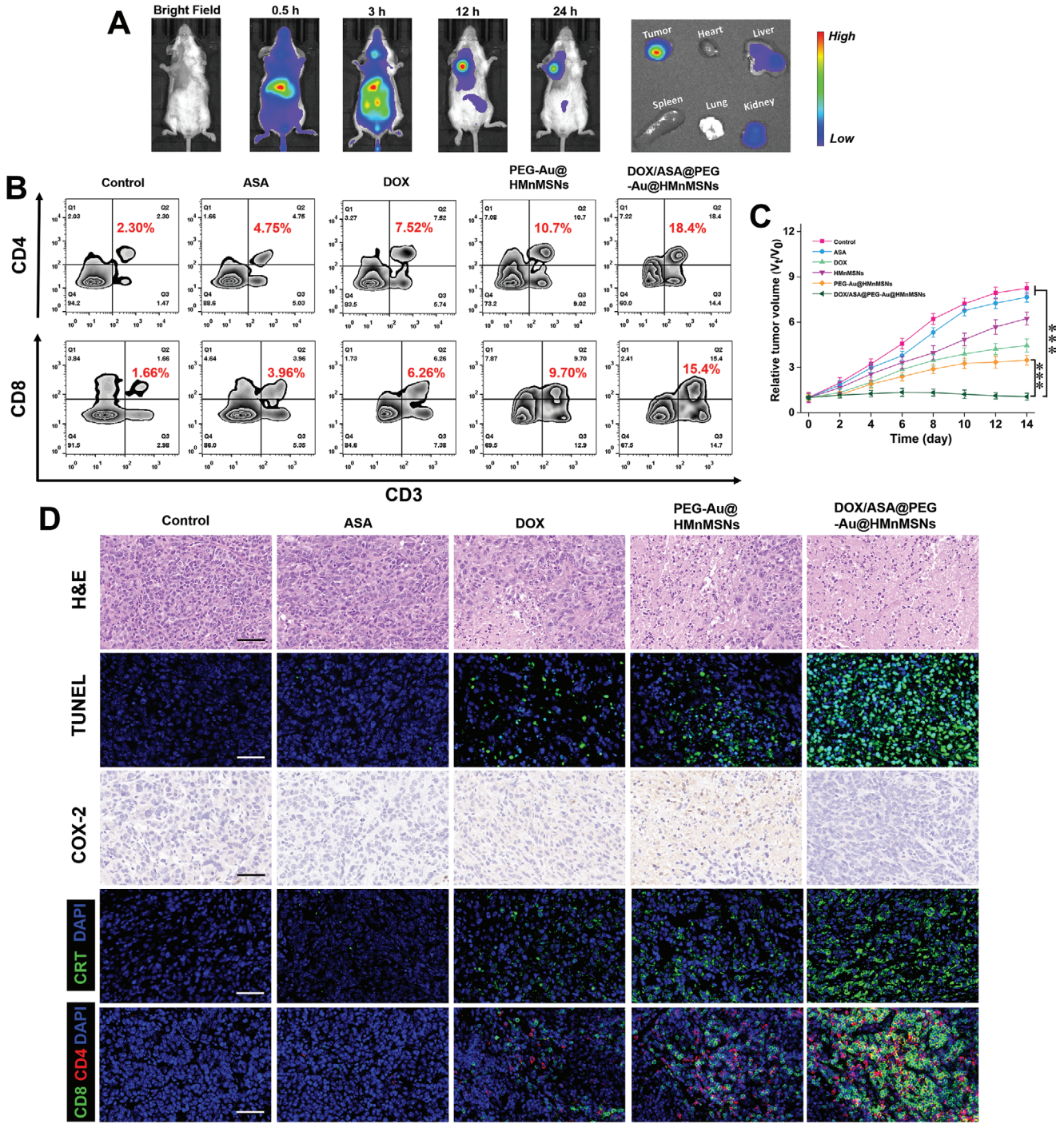

Figure 6. A) In vivo fluorescent images of 4T1 tumor-bearing BALB/c mice after the intravenous injection, and ex vivo fluorescent images of major organs and tumor after 24 h of injection. B) The flow cytometric analysis of the populations of cytotoxic CD8+ and helper CD4+ T cells in 4T1 tumor-bearing BALB/c mice after different treatments. C) Growth curves of tumor volume in tumor-bearing mice with various treatments. D) H&E, TUNEL, and COX-2 staining of tumor slices in different groups. The level of increasing CRT exposure on the tumor sections and the infiltration of CD8+ T cells and CD4+ T cells by immunofluorescence staining assay. Scale bar: 50 µm. $n = 3$, mean ± SD; $^{***}P < 0.001$.

CD8+ and CD4+ staining further verified that DOX/ASA@PEG–Au@HMnMSNs could induce more CD8+/CD4+ cells to activate antitumor immune response, compared with ASA-loaded PEG–Au@HMnMSNs and DOX-loaded PEG–Au@HMnMSNs.

2.9. In Vivo Antitumor Efficacy and Biosafety Evaluation

To reach desirable antitumor efficacy, 4T1 tumor-bearing female BALB/c mice were intravenously injected with different formulations at day 0, 3, 6, and 9. The tumor growth profiles in

Figure 6C; Figure S22, Supporting Information demonstrate that DOX/ASA@PEG–Au@HMnMSNs conduced to robust potential antitumor effect with reduction in tumor volume compared with PBS group, ASA group, HMnMSNs group, DOX groups, and PEG–Au@HMnMSNs group, suggesting the limitation of monotherapy failed to completely suppress the tumor growth. Synergistic GOx-like catalysis-enhanced CDT combined with chemotherapy was further verified by hematoxylin and eosin (H&E) and terminal deoxynucleotidyl transferase dUTP nick-end labeling (TUNEL) staining (Figure 6D). H&E staining images showed bulk necrosis and acellular regions of tumor cells after treatment with DOX/ASA@PEG–Au@HMnMSNs. The TUNEL staining assay exhibited higher cell apoptosis induced by DOX/ASA@PEG–Au@HMnMSNs than other treatments.

In addition, the body weights of the 4T1 tumor-bearing BALB/c mice remained stable after treatments, indicating negligible systemic toxicity (Figure S23, Supporting Information). H&E staining results displayed no obvious physiological morphology changes in the main organs (heart, liver, spleen, lung, and kidney) between control and treatment groups, showing the safety of the formulations (Figure S24, Supporting Information).

3. Conclusion

In summary, we developed biodegradable manganese-doped hollow mesoporous silica coated gold nanoparticles by loading ASA and DOX, as TME-responsive catalytic cascade nanoreactors for enhanced CDT synergistic antitumor chemoimmunotherapy. PEG–Au@HMnMSNs could release Mn^{2+} for Fenton-like reaction to produce $^{\bullet}OH$ through the degradation of GSH in TME, and protect the GOx-like activity of Au to regenerate H_2O_2 for enhanced CDT effect. Such an inherent GO*x*-like catalysis-enhanced CDT combined with DOX treatment could induce sufficient ICD to promote DC maturation and enhance the infiltration of CTLs for systemic antitumor immunity compared with monotherapy. Meanwhile, ASA could recruit DCs and CTLs to tumor sites, restrain the immunosuppressive cells, and remodel ITM by decreasing the expression of PGE_2. This work provided an innovative insight to introduce GOx-like catalytic cascade ICD nano-inducer into potential antitumor immunotherapy with valid remodulation of TME for synergistic tumor therapy.

4. Experimental Section

Materials: Manganese sulfate monohydrate ($MnSO_4{\cdot}H_2O$), cetyltrimethylammonium bromide (CTAB), tetraethyl orthosilicate (TEOS), $HAuCl_4{\cdot}4H_2O$, doxorubicin hydrochloride (DOX·HCl), acetylsalicylic acid (ASA), 3-aminopropyltriethoxysilane (APTES), *N*-hydroxysuccinimide (NHS), *N*-ethylcarbodiimide hydrochloride (EDCl), $mPEG_{2000}$–COOH, methylene blue (MB), glutathione (GSH), hydrogen peroxide (H_2O_2), and glucose were obtained from Sinopharm Chemical Reagent Co., Ltd. 2,2′-Azino-bis(3-ethylbenzothiazoline-6-sulfonic acid) diammonium salt (ABTS), 5,5-dimethyl-1-pyrroline-*N*-oxide (DMPO), peroxidase from horseradish (HRP) (type VI), 5,5′-dithiobis (2-nitrobenzoic acid) (DTNB), and ruthenium dichloride (4, 7-biphenyl-1, 10-phenanthroline) (RDPP) were purchased from Sigma–Aldrich Chemical Company. DCFH–DA, H_2O_2, and GSH assay kit, 4′,6-diamidino-2-phenylindole (DAPI), calcein acetoxymethyl ester/propidium iodide (Calcein-AM/PI), 2″,7″-bis-(2-carboxyethyl)-5-(and-6) carboxy fluorescein, acetoxymethyl ester (BCECF-AM), Cell Counting Kit-8 (CCK-8), and cyclooxygenase 2 monoclonal antibody were supplied from Beyotime Institute of Biotechnology. Antibodies for calreticulin (CRT) were purchased from Bioss Biotech Co., Ltd. Mouse inflammation kit for IL-10, IL-12p70, IL-6, MCP-1, IFN-γ, and TNF-α analysis was purchased from BD Biosciences Co., Ltd. Anti-mouse CD80-PE, anti-mouse CD86-PE-Cyanine5, anti-mouse CD11c-FITC, anti-CD3-PE- Cyanine5, anti-CD4-FITC, and anti-CD8-FITC were obtained from Invitrogen. All other chemicals were of analytical grade and used without further purification.

Preparation of Au@MSNs: Typically, 100 mg of CTAB and 1.2 mL of NaOH (0.5 M) were dissolved in 50 mL of deionized water, and then the solution was heated to 80 °C for 15 min under stirring. 2 mL of formaldehyde solution (3.7 wt%) was added, followed by 1.6 mL of $HAuCl_4$ (0.05 mL) aqueous solution. After stirring for 15 min, an ethanol (1 g) solution of TEOS (0.5 g) was added and the reaction mixture was kept at 80 °C for 1.5 h under stirring. The precipitate was collected via centrifugation at 13 000 rpm for 15 min, washed with water and once with ethanol to remove residual reactants, and finally dried under vacuum. To remove CTAB, the products were stirred for 12 h in a methanol solution of NaCl (1 wt%) for three times. The purple-red products were collected by centrifugation, and then washed with deionized water and ethanol several times, followed by vacuum drying.

Synthesis of PEG–Au@HMnMSNs: To dope manganese in mesoporous silicon, the prepared Au@MSNs were first dispersed into 10 mL of deionized water. Then, 80 mg of $MnSO_4{\cdot}H_2O$ and 100 mg of disodium maleate were dissolved into 10 mL of deionized water. The mixture solution was dropwise added into the Au@MSNs solution and kept for another 30 min under stirring. The final mixture was treated under hydrothermal condition at 180 °C for 13 h. To remove residual reactants, the products were collected by centrifugation, and then rinsed with water and ethanol several times, followed by vacuum drying. The prepared Au@HMnMSNs were further aminated through APTES. Au@HMnMSNs (80 mg) and 450 µL of APTES were refluxed in anhydrous ethanol (30 mL) under magnetic stirring for 24 h. Amine group-modified Au@HMnMSNs were obtained via centrifugation and washed with ethanol. Subsequently, $mPEG_{2000}$—COOH (2.16×10^{-2} mmol), EDCl (1.08×10^{-1} mmol), and NHS (1.08×10^{-1} mmol) were dissolved in 5 mL of anhydrous DMSO and stirred for 4 h to activate the carboxyl groups. 50 mg of aminated Au@HMnMSNs was dispersed in 5 mL of anhydrous DMSO, which was added into the previous activated solution to react for 48 h. The prepared PEG—Au@HMnMSNs were collected via centrifugation, and then washed with deionized water and ethanol.

Preparation of HMnMSNs: Briefly, 200 mg of CTAB and 300 mg of ammonium fluoride were dissolved in 50 mL of deionized water at 80 °C for 15 min under magnetic stirring. Then, 900 µL of TEOS was slowly added dropwise, and the reaction mixture was kept at 80 °C for 2 h. The removal of template was the same as the previous steps, and MSNs were collected via centrifugation. To obtain manganese-doped hollow mesoporous silicon nanoparticles (HMnMSNs), 80 mg of $MnSO_4{\cdot}H_2O$ and 100 mg of disodium maleate were dissolved in 10 mL of deionized water, and then the mixture solution was added into MSNs solution, which was treated under hydrothermal condition at 180 °C for 12 h. The synthesized HMnMSNs were collected via centrifugation, and then rinsed with deionized water several times.

Characterization: Transmission electron microscopy (TEM) and scanning electron microscopy (SEM) images were respectively observed using JEM-2100 transmission electron microscope and field-emission scanning electron microscopy (Zeiss, Ultra Plus). Energy dispersive X-ray spectroscopy (EDS) was carried out on JEM-2100 transmission electron microscope. The valence states of different elements were obtained by X-ray photoelectron spectroscopy (XPS, Thermo Fisher Nexsa). The crystal structure analysis was measured via X-ray diffraction (Ultima IV). The sizes and surface charges of nanoparticles were detected via Brookhaven BI-200SM apparatus. The FTIR and UV–vis adsorption

properties were measured by Thermo Scientific Nicolet 6700 FTIR spectrometer and UV-2600 spectrometer, respectively. The generation of hydroxyl radicals was quantified by an electron spin resonance (ESR) spectrometer using Bruker EMX plus. Thermogravimetric analysis (TGA) was conducted on a TG209 F3 thermogravimetric analyzer. The amount of Mn element was measured by using a TG209 F3 thermogravimetric analyzer. The surface area and pore size distribution of Au@HMnMSNs were further performed on Brunauer–Emmett–Teller Micromeritics Tristar 3000 analyzer.

Drug Loading and Release: In brief, 20 mg of PEG–Au@HMnMSNs and 4 mg of ASA were dispersed in 10 mL of anhydrous DMSO and kept under stirring for 24 h at 25 °C. ASA-loaded PEG–Au@HMnMSNs were collected via centrifugation and washed several times. The as-synthesized ASA-loaded PEG–Au@HMnMSNs were re-dispersed in phosphate buffered saline (PBS) solution containing DOX (4 mg), and the mixture solution stirred for 24 h under dark conditions. ASA/DOX-loaded PEG–Au@HMnMSNs were collected by centrifugation and washed several times. The amounts of ASA and DOX in PEG–Au@HMnMSNs were respectively quantified by TGA and a standard curve via UV–vis spectra. The drug release based on ASA and DOX experiments was measured using a dialysis method in PBS. Equal amounts of ASA/DOX-loaded PEG–Au@HMnMSNs were transferred into dialysis bag (MWCO: 3500 Da) and then incubated into 25 mL of PBS under different conditions (pH 7.4, pH 5.0, pH 5.0 + GSH 5 mM). At predetermined time intervals, the released ASA and DOX were measured by UV–vis spectra.

Degradation Study In Vitro: For the degradation study of PEG–Au@HMnMSNs, certain mass of PEG–Au@HMnMSNs was dispersed in the different GSH concentrations (5 and 8 mM) and pH values (6.8 and 5.0) of simulated body fluid (SBF) solutions, and then stirred gently at 37 °C for scheduled time intervals (6, 12, 24, and 48 h). The mass of released manganese ion and the morphology of PEG–Au@HMnMSNs was respectively determined by ICP-MS analysis and TEM in degradation solutions.

Hemolysis Assay: To obtain standard erythrocyte solution, the blood with EDTA from mouse was collected by centrifugation and resuspended in normal saline. Then, 0.5 mL of erythrocyte suspension was added to 2 mL of normal saline with dispersed ASA/DOX-loaded PEG–Au@HMnMSNs. The mixed solution was centrifuged after 4 h of incubation at 37 °C. Normal saline and deionized water were respectively dissolved in erythrocyte suspension as negative and positive controls. The absorbance (A) value of supernatant was determined at 570 nm by UV–vis spectra. The percentage of hemolysis was calculated as Hemolysis rate (%) = $(A_{\text{sample}} - A_{\text{negative control}})/(A_{\text{positive control}} - A_{\text{negative control}}) \times 100\%$.

GSH Consumption Detection: An indicator 5,5′-dithiobis (2-nitrobenzoic acid) (DTNB) was utilized to determine GSH depletion. Different concentrations of PEG–Au@HMnMSNs (50,100, 200, and 400 μg mL^{-1}) were added to PBS solutions with GSH (pH = 5.0, 8 mM), respectively. Then, the mixtures were kept stirring at 37 °C for 2 h, and supernatants were collected by centrifugation. DTNB solutions were added and the absorbance of supernatants was measured by UV–vis spectra.

Hydroxyl Radical (•OH) Generation by Mn^{2+}-Mediated Fenton-Like Reaction: Methylene blue (MB) was degraded by •OH, which could be used to detect the amount of •OH. PEG–Au@HMnMSNs (80 μg mL^{-1}) were dispersed in $NaHCO_3/CO_2$ buffer solution containing GSH with a series of concentrations (0, 0.5, 1, 5, and 10 mM), and stirred at 37 °C for 6 h. Similarly, PEG–Au@HMnMSNs and 0.5 mM of GSH were dissolved in $NaHCO_3/CO_2$ buffer solution containing glucose with different concentrations (20 and 40 mM). Then, supernatants were collected by centrifugation. 8 mM of H_2O_2 and MB were respectively added supernatants, and further incubated for 15 min. Meanwhile, H_2O_2 and MB with different concentrations of GSH were used as the control groups. The generation of •OH was monitored by the absorbance change of MB at 665 nm and naked eyes.

ESR Measurements: 5,5-dimethyl-1-pyrroline-*N*-oxide (DMPO), as a trapping agent, was employed to determine production of •OH. PEG–Au@HMnMSNs (100 μg mL^{-1}) were dispersed in buffer solution containing GSH with different concentrations (1 and 5 mM) at pH = 7.4 and 5.0, respectively. To investigate the GOx-like catalytic activity of gold nanoparticles, glucose was added to a sample solution. After 4 h of stirring, 8 mM of H_2O_2 and 200 mM of DMPO were added to sample solutions. The •OH characteristic peak signals were measured by ESR spectrometer.

GOx-Like Activity of PEG–Au@HMnMSNs: A horseradish peroxidase (HRP)-based colorimetric measurement was utilized to investigate the enzymatic activity of Au nanozyme. Briefly, a mixed solution of 100 μg mL^{-1} of PEG–Au@HMnMSNs solution in 10 mM NaCl and 10 mM Tris-HCl buffer in 100 mM NaCl was incubated with 100 mM glucose for 30 min. Then, the supernatant was collected by centrifugation to avoid the color interference. Subsequently, the supernatant was added to 50 mM Tris-HCl buffer solution containing HRP (5 μg mL^{-1}) and ABTS (1 mM). The resulting solution continued to incubate for 10 min before measurement of absorbance at 405 nm by UV–vis spectra.

Cell Culture: In this study, Murine breast cancer (4T1) cells were incubated in RPMI 1640 complete medium containing 10% FBS and 1% penicillin–streptomycin solution, and all cell lines were cultured under a humidified atmosphere containing 5% CO_2 at 37 °C.

Cellular Uptake Study: 4T1 cells were seeded into confocal petri dishes and 6-well plates at a density of 1×10^5 cells and incubated for 24 h. Then, the cells were cultured with DOX-loaded PEG–Au@HMnMSNs at 2 μg mL^{-1} of DOX. The cellular uptake was obtained by CLSM and flow cytometry at predetermined time intervals. DAPI was employed to locate cell nucleus before observation by CLSM.

Chemodynamic Activity In Vitro: DCFH–DA assay was employed to qualitatively and quantitatively detect the ROS levels mediated by Mn^{2+}-based GOx-catalysis enhanced chemodynamic activity. 4T1 cells were seeded into confocal petri dishes and 6-well plates at a density of 1×10^5 cells and incubated for 24 h. Then, the medium was replaced with PEG–Au@HMnMSNs (60 μg mL^{-1}) for different incubation times (1, 6, and 12 h). In addition, the medium was also replaced with PEG–Au@MSNs, PEG–-HMnMSNs, and PEG–Au@HMnMSNs for 6 h of incubation. The cells were washed with PBS and incubated with DCFH–DA solution for 15 min. Dyed cells were observed with CLSM. To quantitatively examine the level of ROS, the cells were incubated with PEG–Au@HMnMSNs, ASA/DOX-loaded PEG–Au@HMnMSNs, and ASA/DOX-loaded PEG–Au@HMnMSNs plus glucose (50 mM) at 37 °C for another 8 h. The cells were collected and analyzed by flow cytometry.

Intracellular pH Detection: Cascade nanozyme was expected to catalyze glucose to produce H_2O_2 and gluconic acid, and consume oxygen. BCECF AM could be quenched at acidic environment. After 4T1 cells incubation with medium, HMnMSNs, and PEG–Au@HMnMSNs in confocal petri dishes and 6-well plates, fresh medium containing 5 μM of BCECF AM was added and cultured for another 1 h. The dyed 4T1 cells were observed by CLSM and resuspended in PBS solution for flow cytometry analysis.

Intracellular O_2 Assay: RDPP, as oxygen probe, was employed to detect the level of intracellular O_2. 4T1 cells were seeded into confocal petri dishes at a density of 1×10^5 cells and incubated for 24 h. The medium was replaced with fresh medium, HMnMSNs, and PEG–Au@HMnMSNs for 8 h. After removal of medium, fresh medium containing RDPP was added and cultured for another 4 h. Finally, the cells were observed by CLSM.

Intracellular H_2O_2 Measurement: To detect the level of H_2O_2 in vitro, 4T1 cells were seeded into 96-well plates overnight at a density of 5×10^3 per well and then treated with different formulations (ASA, DOX, PEG–Au@HMnMSNs, and DOX/ASA-loaded PEG-Au@HMnMSNs). The level of H_2O_2 was tested via H_2O_2 assay kit according to the manufacturer's instructions after incubation for 24 h.

Cytotoxicity Evaluation in Vitro: In brief, 4T1 cells (6×10^3 per well) were seeded into 96-well plates and cultured for 24 h. Subsequently, the medium was replaced with fresh medium containing various concentration of PEG–HMnMSNs, PEG–Au@MSNs, PEG–Au@HMnMSNs, ASA, DOX, and ASA/DOX-loaded PEG–Au@HMnMSNs ($\text{Mass}_{\text{Nanoparticle}}$: 12.5, 25, 50, 100, and 200 μg mL^{-1}). After 24 h of incubation, 10 μL CCK-8 was added and treated for another 1 h. A microplate reader was used for measurements at 450 nm.

Cell Apoptosis: 4T1 cells (1×10^5 cells per well) seeded into 6-well plates were cultured for 24 h. Then, 4T1 cells were washed by PBS solutions and treated with PEG–Au@HMnMSNs (25, 50, and 100 μg mL^{-1}) for 24 h. The 4T1 cells were digested, washed, and resuspended with 500 μL buffer solution. After staining with Annexin-V-FITC and PI for 15 min in the dark, cell apoptosis was analyzed by flow cytometry.

Cell Live–Dead Staining Experiments: To further investigate the survival and death of cells, 4T1 cells (1×10^5 cells per well) seeded into 6-well plates were cultured for 24 h. Then, the cells were incubated with PEG–Au@HMnMSNs, DOX/ASA, and DOX/ASA-loaded PEG–Au@HMnMSNs at 60 μg mL^{-1} of nanoparticles. After staining with Calcein-AM and PI for 30 min, the treated cells were observed by CLSM.

Western Blotting for the COX-2 Protein: 4T1 and RAW264.7 cells were seeded into 6-well plates and cultivated for 24 h. After RAW264.7 cells stimulation with LPS, the 4T1 and RAW264.7 cells were incubated with various concentrations of ASA. Then, 4T1 cells were treated with fresh medium, PEG–Au@HMnMSNs, DOX, ASA, and DOX/ASA-loaded PEG–Au@HMnMSNs for 12 h. The cells were collected by trypsin digestion and washed with PBS. Total proteins were extracted by RIPA lysis buffer, and the level of COX-2 protein was detected via western blot analysis.

PGE_2 Level Analysis In Vitro: To further measure the mass of PGE_2 in vitro, 4T1 and RAW264.7 cells were incubated overnight, and then treated with fresh medium, PEG–Au@HMnMSNs, DOX, ASA, and DOX/ASA-loaded PEG–Au@HMnMSNs. The mass of PGE_2 in the supernatants were performed on a PGE_2 ELISA Kit according to the manufacturer's instructions.

Induced DAMP Release In Vitro: To detect GOx-like catalysis enhanced chemodynamic therapy combined with chemotherapy-induced ICD of the 4T1 cells, CRT exposure and expression of HMGB1 were investigated in vitro. 4T1 cells were seeded into 6-well plates and incubated with fresh medium, HMnMSNs, DOX/ASA, PEG–Au@HMnMSNs, and DOX/ASA-loaded PEG–Au@HMnMSNs at 50 μg mL^{-1} of nanoparticles, respectively. The cells were collected, washed, and cultured with Alexa Fluor 488-conjugated anti-CRT antibody for 20 min for flow cytometry analysis. For CLSM observation, 4T1 cells were incubated with fresh medium, HMnMSNs, DOX/ASA, PEG–Au@HMnMSNs, and DOX/ASA-loaded PEG–Au@HMnMSNs. The cells were stained with Alexa Fluor 488-conjugated anti-CRT antibody before observation.

To detect the release of HMGB1 in the supernatants corresponding to the samples tested by the above CRT experiments, the amounts of HMGB1 in the supernatants were performed on a HMGB1 ELISA Kit according to the manufacturer's instructions. In addition, 4T1 cells were collected to measure the level of HMGB1 protein using HMGB1 rabbit monoclonal antibody by western blot after incubation with DOX/ASA-loaded PEG–Au@HMnMSNs (25 and 50 μg mL^{-1}).

ICD-Induced Immune Activation In Vitro: Briefly, bone marrow-derived dendritic cells (BMDCs) were obtained from primary bone marrow cells of female BALB/c mice, and BMDCs were seeded into 24-well plates. 4T1 cells were seeded into 24-well plates and cultured for 24 h. Then, the cells were treated with fresh medium, ASA, DOX, PEG–Au@HMnMSNs, and DOX/ASA-loaded PEG–Au@HMnMSNs at 50 μg mL^{-1} of nanoparticles for 12 h. Each group-conditioned supernatant was added into BMDCs and incubated for 24 h. The stimulated BMDCs were detected using anti-mouse CD80-PE, anti-mouse CD86-PE-Cyanine5, and anti-mouse CD11c-FITC by flow cytometry. Each supernatant was used to determine the level of IL-10, IL-12p70, IL-6, IFN-γ, and TNF-α using mouse inflammation kit for IL-10, IL-12p70, IL-6, IFN-γ, and TNF-α analysis.

In Vivo Biodistribution and Imaging Studies: 4T1 tumor-bearing female BALB/c mice were intravenously administrated with Cy5.5-labeled PEG–Au@HMnMSNs. The biodistribution and fluorescent intensity were observed by IVIS small animal imaging system at predetermined time intervals. Moreover, the fluorescent intensity major organs (heart, liver, spleen, lung, and kidney) were obtained at a certain time interval. All animal experimental procedures were approved by the Experimental Animal Ethics Committee of Southeast University guidelines (China). All animal experiments followed the institutional guidelines of the Experimental Animal Ethics Committee of Southeast University (China) and were performed in compliance with the regulations for the Administration of Affairs Concerning Experimental Animals of China.

In Vivo Antitumor Efficacy: 4T1 tumor-bearing female BALB/c mice were randomly divided into six groups ($n = 3$) when the volume of tumor reached 60 mm^3. The mice were intravenously injected with PBS, ASA (0.32 mg kg^{-1}), DOX (0.5 mg kg^{-1}), HMnMSNs (4 mg kg^{-1}), PEG–Au@HMnMSNs (4 mg kg^{-1}), and DOX/ASA-loaded PEG–Au@HMnMSNs (4 mg kg^{-1}) at day 0, 3, 6, and 9. The tumor size (length: L and width W) and body weight were recorded every 2 days. Tumor volume (V) and relative tumor were calculated as $V = (L \times W^2)/2$ and V_t/V_0 (0: day 0, t: day t), respectively. The treated mice were sacrificed to harvest main organs for H&E staining, and the obtained tumors from different groups of mice were sliced for H&E staining, terminal deoxynucleotidyl TUNEL staining, immunohistochemical staining of COX-2, and immunofluorescence staining.

The Detection of CD4+ and CD8+ T Lymphocytes in Vivo: To examine the infiltration of T cells in tumor, saline, ASA, DOX, PEG–Au@HMnMSNs, and DOX/ASA-loaded PEG–Au@HMnMSNs were intratumorally injected into 4T1 tumor-bearing BALB/c mice at day 0, 3, and 6. After the final treatments, the tumors were harvested, cut into several small pieces, and homogenized to obtain a single-cell suspension. Then, the cells were washed with PBS and stained with anti-CD3-PE-Cyanine5, anti-CD4-FITC, and anti-CD8-FITC followed by flow cytometry analysis.

Statistical Analysis: All the data are expressed as the mean ± standard deviation (SD). Analysis of variance (ANOVA) within GraphPad Prism 8.0 software (San Diego, CA, USA) was used to confirm statistically significant differences between groups. Statistical significances were determined using Student's t test, with the following P values considered significant: $^*P < 0.05$, $^{**}P < 0.01$, and $^{***}P < 0.001$.

Supporting Information

Supporting Information is available from the Wiley Online Library or from the author.

Acknowledgements

This work was financially supported by the National Natural Science Foundation of China (81771976), the National Key Research and Development Program of China (Grant 2018YFC1901202), the State Key Laboratory of Pathogen and Biosecurity (Academy of Military Medical Science SKLPBS2134), the Fundamental Research Funds for the Central Universities, and the joint fund of Southeast University and Nanjing Medical University.

Conflict of Interest

The authors declare no conflict of interest.

Data Availability Statement

The data that support the findings of this study are available from the corresponding author upon reasonable request.

Keywords

cascade reaction, chemodynamic therapy, dendritic cells, immune system activation, immunogenic cell death

Received: March 31, 2021
Revised: June 9, 2021
Published online:

[1] S. Yan, Z. Luo, Z. Li, Y. Wang, J. Tao, C. Gong, X. Liu, *Angew. Chem., Int. Ed.* **2020**, *59*, 17332.
[2] X. Li, X. Cai, Z. Zhang, Y. Ding, R. Ma, F. Huang, Y. Liu, J. Liu, L. Shi, *Nano Lett.* **2020**, *20*, 4454.
[3] M. Wen, J. Ouyang, C. Wei, H. Li, W. Chen, Y. N. Liu, *Angew. Chem., Int. Ed.* **2019**, *58*, 17425.
[4] F. Gao, Y. Tang, W. L. Liu, M. Z. Zou, C. Huang, C. J. Liu, X. Z. Zhang, *Adv. Mater.* **2019**, *31*, 1904639.
[5] L. Galluzzi, A. Buque, O. Kepp, L. Zitvogel, G. Kroemer, *Nat. Rev. Immunol.* **2017**, *17*, 97.
[6] A. D. Garg, P. Agostinis, *Immunol. Rev.* **2017**, *280*, 126.
[7] Q. Chen, L. Liu, Y. Lu, X. Chen, Y. Zhang, W. Zhou, Q. Guo, C. Li, Y. Zhang, Y. Zhang, D. Liang, T. Sun, C. Jiang, *Adv. Sci.* **2019**, *6*, 1802134.
[8] Y. Liu, N. Qiu, L. Shen, Q. Liu, J. Zhang, Y. Y. Cheng, K. H. Lee, L. Huang, *J. Controlled Release* **2020**, *323*, 431.
[9] Z. Dai, J. Tang, Z. Gu, Y. Wang, Y. Yang, Y. Yang, C. Yu, *Nano Lett.* **2020**, *20*, 6246.
[10] M. Chang, M. Wang, M. Wang, M. Shu, B. Ding, C. Li, M. Pang, S. Cui, Z. Hou, J. Lin, *Adv. Mater.* **2019**, *31*, 1905271.
[11] J. An, K. Zhang, B. Wang, S. Wu, Y. Wang, H. Zhang, Z. Zhang, J. Liu, J. Shi, *ACS Nano* **2020**, *14*, 7639.
[12] C. Riera-Domingo, A. Audige, S. Granja, W.-C. Cheng, P.-C. Ho, F. Baltazar, C. Stockmann, M. Mazzone, *Physiol. Rev.* **2020**, *100*, 1.
[13] K. Ni, T. Luo, G. T. Nash, W. Lin, *Acc. Chem. Res.* **2020**, *53*, 1739.
[14] Y. Liu, T. Lang, Z. Zheng, H. Cheng, X. Huang, G. Wang, Q. Yin, Y. Li, *Small* **2019**, *15*, 43.
[15] S. Zelenay, A. G. van der Veen, J. P. Bottcher, K. J. Snelgrove, N. Rogers, S. E. Acton, P. Chakravarty, M. R. Girotti, R. Marais, S. A. Quezada, E. Sahai, C. R. E. Sousa, *Cell* **2015**, *162*, 1257.
[16] Y. Wang, W. Song, M. Hu, S. An, L. Xu, J. Li, K. A. Kinghorn, R. Liu, L. Huang, *Adv. Funct. Mater.* **2018**, *28*, 1802847.
[17] P. Kalinski, *J. Immunol.* **2012**, *188*, 21.
[18] N. Obermajer, R. Muthuswamy, J. Lesnock, R. P. Edwards, P. Kalinski, *Blood* **2011**, *118*, 5498.
[19] B. Yang, J. Shi, *Angew. Chem., Int. Ed.* **2020**, *59*, 49.
[20] D. A. Drew, Y. Cao, A. T. Chan, *Nat. Rev. Cancer* **2016**, *16*, 173.
[21] D. Liao, L. Zhong, T. M. Duan, R. H. Zhang, X. Wang, G. Wang, K. S. Hu, X. B. Lv, T. B. Kang, *Clin. Cancer Res.* **2015**, *21*, 5349.
[22] Y. Cao, R. Nishihara, Z. R. Qian, M. Y. Song, K. Mima, K. Inamura, J. A. Nowak, D. A. Drew, P. Lochhead, K. Nosho, T. Morikawa, X. H. Zhang, K. N. Wu, M. L. Wang, W. S. Garrett, E. L. Giovannucci, C. S. Fuchs, A. T. Chan, S. Ogino, *Gastroenterology* **2016**, *151*, 879.
[23] W. Song, L. Shen, Y. Wang, Q. Liu, T. J. Goodwin, J. Li, O. Dorosheva, T. Liu, R. Liu, L. Huang, *Nat. Commun.* **2018**, *9*, 2237.
[24] R. Kuai, W. Yuan, S. Son, J. Nam, Y. Xu, Y. Fan, A. Schwendeman, J. J. Moon, *Sci. Adv.* **2018**, *4*, 1736.
[25] S. Chen, D. Li, X. Du, X. He, M. Huang, Y. Wang, X. Yang, J. Wang, *Nano Today* **2020**, *35*, 100924.
[26] M. Comotti, C. D. Pina, R. Matarrese, M. Rossi, *Angew. Chem., Int. Ed.* **2004**, *43*, 5812.
[27] W. Luo, C. Zhu, S. Su, D. Li, Y. He, Q. Huang, C. Fan, *ACS Nano* **2010**, *4*, 7451.
[28] X. Liu, Y. Pan, J. Yang, Y. Gao, T. Huang, X. Luan, Y. Wang, Y. Song, *Nano Res.* **2020**, *13*, 653.
[29] S. Gao, H. Lin, H. Zhang, H. Yao, Y. Chen, J. Shi, *Adv. Sci.* **2019**, *6*, 1801733.
[30] S. Dong, J. Xu, T. Jia, M. Xu, C. Zhong, G. Yang, J. Li, D. Yang, F. He, S. Gai, P. Yang, J. Lin, *Chem. Sci.* **2019**, *10*, 4259.
[31] L. Yu, Y. Chen, M. Wu, X. Cai, H. Yao, L. Zhang, H. Chen, J. Shi, *J. Am. Chem. Soc.* **2016**, *138*, 9881.
[32] R. Deng, X. Xie, M. Vendrell, Y. T. Chang, X. Liu, *J. Am. Chem. Soc.* **2011**, *133*, 20168.
[33] Y. Zhang, C. Teh, M. Li, C. Y. Ang, S. Y. Tan, Q. Qu, V. Korzh, Y. Zhao, *Chem. Mater.* **2016**, *28*, 7039.
[34] L. S. Lin, J. Song, L. Song, K. Ke, Y. Liu, Z. Zhou, Z. Shen, J. Li, Z. Yang, W. Tang, G. Niu, H. H. Yang, X. Chen, *Angew. Chem., Int. Ed.* **2018**, *57*, 4902.
[35] H. Wu, F. Chen, C. You, Y. Zhang, B. Sun, Q. Zhu, *Small* **2020**, *16*, 2001805.
[36] K. Sun, Z. Gao, Y. Zhang, H. Wu, C. You, S. Wang, P. An, C. Sun, B. Sun, *J. Mater. Chem. B* **2018**, *6*, 5876.
[37] B. Feng, Z. Niu, B. Hou, L. Zhou, Y. Li, H. Yu, *Adv. Funct. Mater.* **2019**, *30*, 1906605.
[38] Q. Chen, J. Chen, Z. Yang, J. Xu, L. Xu, C. Liang, X. Han, Z. Liu, *Adv. Mater.* **2019**, *31*, 1802228.
[39] W. Yang, G. Zhu, S. Wang, G. Yu, Z. Yang, L. Lin, Z. Zhou, Y. Liu, Y. Dai, F. Zhang, Z. Shen, Y. Liu, Z. He, J. Lau, G. Niu, D. O. Kiesewetter, S. Hu, X. Chen, *ACS Nano* **2019**, *13*, 3083
[40] Y. P. Jia, K. Shi, F. Yang, J. F. Liao, R. X. Han, L. P. Yuan, Y. Hao, M. Pan, Y. Xiao, Z. Y. Qian, X. W. Wei, *Adv. Funct. Mater.* **2020**, *30*, 2001059.